Bulgarian Chemical Communications, Volume 48, Number3 (pp. 430– 439) 2016

Structural, magnetic and catalytic properties of Co substituted manganite nano-perovskites

A. Gholizadeh[1*], A. Malekzadeh[2], M. Ghiasi[2]

[1]*School of Physics, Damghan University (DU), Damghan, I.R. Iran*
[2]*School of Chemistry, Damghan University (DU), Damghan, I.R. Iran*

Received August 4, 2015, Revised October 22, 2015

In this work, structural, magnetic and catalytic properties of $LaMn_{1-x}Co_xO_3$ (x = 0.00, 0.25, 0.50, 0.75, 1.00) are investigated. The structural characterization of the samples by X-ray powder diffraction and using the X'Pert package and Fullprof program is evidence for a monoclinic structure (P21/n space group) with x = 0.5 and a rhombohedral structure (R-3c space group) for other samples. These results have been confirmed by FTIR measurements. The magnetic characterizations of the samples have been studied by magnetization measurement versus temperature and field. The structural and magnetic results show the ferromagnetic interactions of Co^{2+}–Mn^{4+} for $x \leq 0.5$ are being progressively replaced by the less effective Co^{2+}–Co^{3+} and Mn^{4+}-Co^{3+} interactions for $x > 0.5$. The catalytic activity of $LaMn_{1-x}Co_xO_3$ was evaluated for C_2H_6 combustion and CO oxidation reactions. Under similar reaction conditions, the catalytic results show that the $LaMn_{0.5}Co_{0.5}O_3$ nano-perovskite is the best catalyst for C_2H_6 combustion and CO oxidation.

Keywords: Nano-Perovskite; Manganite-Cobaltite; Structural and Magnetic Phase Transition; C_2H_6 combustion; CO oxidation.

INTRODUCTION

Many efforts have been made to reduce the use of precious metals in catalysts (Pt, Pd and Rh), and use new compounds which are cheaper and have a better catalytic activity. Finding a suitable replacement for expensive catalysts used in various industries, including the automotive industry, to further reduce the environmental pollutants emitted is a major research endeavor in the modern world. A high activity in the reduction-oxidation (redox) reaction, oxygen storage capability and high flexibility in including other metals in the structure, have proposed perovskite compounds ABO_3 as a good candidate for this replacement. In addition, being inexpensive and having heat and mechanical resistance properties are some other advantages of these compounds. Among perovskite compounds, lanthanum manganites and cobaltites with formulas $LaMnO_3$ and $LaCoO_3$ are the famous compounds that are used to complete the oxidation reaction of CO and hydrocarbons [1-2].

$LaMn(Co)O_3$ with a perovskite structure is an insulator-antiferromagnetic at room temperature due to the absence of ions Mn^{4+} (Co^{4+}). With the replacement of the La^{3+} ions by bivalent elements (Sr, Ca, …), the trivalent ions Mn (Co) are converted to a mixture of ions Mn^{3+} and Mn^{4+} (Co^{3+} and Co^{4+}). The measurements reported on polycrystalline samples of $La_{1-y}M_yMn(Co)O_3$, showed an insulator-antiferromagnetic behavior for low and high values of y and metal-ferromagnetic behavior at the concentration $y \approx 1/3$ [3-4]. In these compounds, the ferromagnetic-paramagnetic transition associated with a metal-insulator transition below the curie temperature ($100 < T_C\,(K) < 350$) has been attributed to the double-exchange theory between the ions Mn^{3+}-Mn^{4+} (Co^{3+}-Co^{4+}) [5]. In manganite-cobaltite $LaMn_{1-x}Co_xO_3$, the origin of the metal-ferromagnetic behavior is due to ferromagnetic interaction between the ions of Mn^{3+}-Mn^{3+} and Mn^{4+}-Co^{2+} [6]. Furthermore, all the electronic, magnetic and redox properties of the samples will depend on the nature of the interaction between the Co and Mn ions via oxygen.

Several investigators [5-8] have reported that in ABO_3 perovskites, the *A* ions in general are catalytically inactive and the active ions at the *B* position readily interact with the gas molecules. It shoud be noted that the substitution at the A-site with a bivalent cation or a tetravalent cation leads to a different behavior of the catylytic activity of manganite-cobaltie compounds. Because the B-O bond lengh and the bond energy depend on the lattice parameter this alters the $B\text{-}O_{ad}$ [5]. The Sr substitution for La in $La_{1-y}A_yCoO_3$ leads to higher oxidation states for Co, so that the higher the amount of Sr, the higher is the concentration of Co^{4+} [8]. However, since Co^{4+} is unstable, then oxygen relase can take place ending in the formation of oxygen vacancies that leads to a

* To whom all correspondence should be sent:
E-mail: gholizadeh@du.ac.ir; ah_gh1359@yahoo.com

decrease of the catalytic activity. By contrast, the insertion of Ce^{4+} in $La_{1-y}A_yCoO_3$ leads to a partial reduction of Co^{3+} to Co^{2+}, thus affording a large amount of active sites for oxgen adsorption from the gas-phase that leads to an increase in catylytic activity [5].

The changes in the $AB_{1-x}B'_xO_3$ perovskite catalytic properties of the substituting cation B with B' can be classified in two categories: geometric and electronic structure of cation B' [6]. The effect of B' substitution on geometric and electronic factors is considered in the calculation of the structural and magnetic changes.

In this work, we prepared $LaMn_{1-x}Co_xO_3$(x = 0.00, 0.25, 0.50, 0.75, 1.00) by the citrate precursor method and tried to explain the structural and magnetic properties and the influence of Co substitution on their catalytic activities for C_2H_6 combustion and CO oxidation reactions by using reasonable experimental data.

EXPERIMENTAL

The $LaMn_{1-x}Co_xO_3$ compounds with x = 0.00, 0.25, 0.50, 0.75, and 1.00 were prepared by the citrate precursor method, similar to the recipe reported elsewhere [9]. First, a solution containing appropriate concentrations of metal nitrates $La(NO_3)_3{\cdot}6H_2O$, $Mn(NO_3)_2{\cdot}4H_2O$, $Co(NO_3)_2{\cdot}6H_2$ and citric acid, equal to the total number of moles of nitrate ions, was evaporated at 60°C, overnight. The homogeneous sol-like substance was subsequently dried at 80°C, overnight. The resulting spongy and friable materials were completely powdered and kept at 200°C, overnight. The resulting materials were powdered again and calcined at 600°C for 5 h. The samples were subsequently calcined for 5 more hours at 900°C.

The X-ray diffraction (XRD) patterns have been recorded using a Bruker AXS diffractometer D8 ADVANCE with Cu-Kα radiation in the range 2θ = 20-80° at room temperature (RT). The XRD data was analyzed using a commercial X'pert package and the Fullprof program.

XRD profile analysis is a simple and powerful method to evaluate the crystallite size and lattice strain. Two factors determine the breadth of the Bragg peak including the crystallite size-dependent (β_D) or strain dependent broadening (β_S) effects, except for the instrument-dependent effect. To do an accurate analysis for size and strain effects, the instrumental broadening must be accounted for. Scherrer's equation is as follows:

$$D = \frac{0.94\,\lambda}{\beta_{hkl}\cos\theta}\ , \qquad (1)$$

This shows the broadening of the XRD pattern which is attributed to the crystallite size-induced broadening. Here, β_{hkl} is the full-width at half-maximum of the diffraction peaks. The information on strain (ε) and crystallite size (D) of the powders have been obtained from β_{hkl} and the planar spacing d_{hkl} via the Halder-Wagner method [10]:

$$\left(\frac{\beta^*_{hkl}}{d^*_{hkl}}\right)^2 = \left(\frac{1}{D}\right)\left(\frac{\beta^*_{hkl}}{d^{*\,2}_{hkl}}\right) + \left(\frac{\varepsilon}{2}\right)^2 , \quad (2)$$

where $\beta^*_{hkl} = \beta_{hkl}cos\theta/\lambda$ and $d^*_{hkl} = 2sin\theta/\lambda$. Finally, the results of the Halder-Wagner method are compared with the Scherrer method.

The FT-IR spectra were recorded in a Perkin-Elmer spectrum RXI-IR spectrometer, operating by ratio, single beam, or interferogram mode, in the range 400-1500 cm^{-1}. The samples were finely ground in an agate mortar with KBr as diluent and pelleted for the IR analysis. The morphology of the samples was studied by SEM (Philips XL30) analysis. The particle size of the samples was investigated by TEM (LEO Model 912AB) analysis.

The absorption coefficient is a suitable quantity for studying the band gap energy. Optical absorption spectra of $LaMn_{1-x}Co_xO_3$ between 200 and 1100 nm wavelengths have been recorded at room temperature using a HP-UV–Vis system (Agilent8453, model). The band gap energies have been calculated in accordance with Ref. [11]. The following relation holds between the optical absorption coefficient, α (λ), and the optical band gap energy of a direct band transition [25]:

$$(\alpha h\nu)^2 = B(h\nu - E_g) \quad (3)$$

where B is an energy-independent constant and $\alpha(\lambda) = 2.303\,A(\lambda)/t$ is the optical absorption coefficient calculated from the absorption spectra ($A(\lambda)$) is the mean particle size of the sample (t). The band gap energy of the samples is estimated by extrapolating the linear part of $(\alpha h\nu)^2$ vs. a $h\nu$ plot. The hysteresis loops at 10 K and temperature dependence of magnetization between 10-400 K was carried out in a SQUID magnetometer (Quantum Design, Inc.). The magnetization curve in high fields can usually be fitted by the empirical formula; law of approach to saturation [12]:

$$M(H) = M_s[1 - (a/H) - (b/H^2) - (c/H^3)] + \chi H + EH^{1/2} \ , (4)$$

where $M(H)$ and M_S are the magnetization at the field H and the saturation magnetization explained by atomic theory, respectively.

Catalytic tests for C_2H_6 combustion and CO oxidation reactions over $LaMn_{1-x}Co_xO_3$ catalysts were studied in an experimental set-up using a quartz tube, filled with 200 mg of a 60-100 mesh sized catalyst supported on ceramic wool under GHSV of 12,000 h^{-1}. In a typical experiment, a model exhaust gas obtaining a mixture of 6 vol% CO and 0.2 vol% C_2H_6 as a hydrocarbon (HC) model compound, in Ar and air (a stoichiometric ratio with respect to oxygen) was passed through the catalyst bed with a total gas mixture flow rate of 40 mL/min at STP. Catalytic test studies were carried out by temperature rising in random intervals from 50°C to the complete oxidation temperature. The product stream was analyzed by a GC on a FI detector.

RESULTS AND DISCUSSIONS

Structural and morphologic properties

X-ray diffraction patterns of $LaMn_{1-x}Co_xO_3$ (x = 0.00, 0.25, 0.50, 0.75, 1.00), are shown in Fig. 1. The XRD data were analyzed using both the commercial X'Pert High Score package and the Fullprof program. Identification of the structure type using the X'pert package confirms the perovskite structure in all samples without a presence of impurity phases. As shown in the XRD pattern of samples x = 0.00, 0.25, 0.75, 1.00 (Fig. 1), a splitting of the peaks of the perovskite at angles ~33°, ~41°, ~58°, ~68° and ~78° is an indication of a rhombohedral system [13]. Also, for a better comparison, a peak at about ~33° is shown in the inset of Fig. 1. For x = 0.00, the peak at ~33° is a very intense doublet, while for other samples it is fully split. These results for x = 0.00 suggest a mixture of $LaMnO_3$ and $LaMnO_{3+\delta}$ with cubic and rhombohedral structures, respectively. However, the XRD pattern of sample x = 0.50 is different, while more broadening of the peaks mentioned above and a splitting of the peak at the angle ~47° indicate a lower symmetry.

Results of the Rietveld analysis using the Fullprof program indicate that all the diffraction peaks of the sample at x = 0.50 can be quite well indexed in the monoclinic structure (space group $P2_1/n$) and for other samples in the Rhombohedral structure (space group R-3c). Also, the results of the Rietveld analysis using the Fullprof program indicate that the best fit with the least difference was carried out (Fig. 1). To perform a Rietveld refinement we need good initial values for the lattice parameters and the type of space group obtained from a phase analysis of the X'pert package.

The hexagonal cell is no longer primitive and has three times the volume of the rhombohedral cell. When the XRD pattern of a rhombohedral sample is indexed, i.e., with reference to hexagonal axes and the true nature of the lattice determined, we usually want to know the lattice parameters a_r and α of the rhombohedral unit cell. But the dimensions of the rhombohedral cell can be determined from the dimensions of the hexagonal cell and this is an easier process than solving the rather complicated plane-spacing equation for the rhombohedral system. The first step is to analyze and index the XRD pattern on the basis of the hexagonal axes using the Fullprof program. Then, the parameters a_H and c of the hexagonal cell are calculated in the usual way. Finally, the parameters a_r and α of the rhombohedral cell are determined from the refined parameters a_H and c of the hexagonal cell using the Fullprof program according to the following equations:

$$a_r = \frac{1}{3}\sqrt{3a_H^2 + c^2}, \quad \sin\frac{\alpha}{2} = \frac{3}{2\sqrt{3+(c/a_H)^2}}, \quad (5)$$

The derived lattice parameters of the samples for rhombohedral and monoclinic structures are given in Table 1. It should be noted that if the c/a_H ratio of the hexagonal cell takes on the special value of 2.45, then the angle α of the rhombohedral cell will be equal to 60° and the bond angle *B*-O-*B* is 180°. Consequently, the lattice points will be face-centered cubic (*t* is equal to 1). Also, the magnitude of the rotation of BO_6 can be evaluated from either the angle α of the rhombohedral unit cell written in Table 1or from the axial ratio c/a_H of the hexagonal cell. As a result of the rotation (tilting), the B-O-B bond angle (≤180°) and α deviate from the ideal perovskite value. Notice, that for trigonal angles, α, is less than 60 degrees, the transformation can be achieved by an expansion along the body diagonal [111] of the Rhombohedral or along the c-axis [001] of the hexagonal; while, for trigonal angles this is greater than 60 degrees, a contraction in the body diagonal [111] of the Rhombohedral or along the c-axis [001] of the hexagonal. Therefore, the obtained values of the angle α are higher than 60° this means the BO_6 octahedron is slightly compressed along the (hexagonal *c* axis) rhombohedral (111) axis with respect to the cubic structure.

From the X-ray diffraction patterns at about 33° shown in the inset of Fig. 1, two tendencies are

observed for values of $x \leq 0.50$ and $x > 0.50$. For values of $x \leq 0.50$, the peaks shift is nearly constant upon increasing the Co-content and means a slight increase of the unit cell volume. But for values of $x > 0.50$, an increase of peaks shifts to larger 2θ, consequently a decrease of the unit cell volume is observed with the degree of substitution. These findings are in accordance with the refined unit cell volume obtained from the Rietveld method using the Fullprof program summarized in Table 1.

There is no apparent linear correlation between the perovskite structure, the substitution degree and that for x = 0.50 when the transformation of the crystal phase occurs. This is due to the substitution of Mn^{x+} ions in the lattice by Co^{x+} ions. Therefore, all these findings should be correlated with the ionic radii of each one of the components. The presence of several ionic states (Mn^{3+}, Mn^{4+}, Co^{2+} and Co^{3+}) makes it difficult to decide just from the XRD data.

Table 1. The structure type and unit cell parameters of $LaMn_{1-x}Co_{x3.}$

Sample	Structure (space group)	lattice Parameters	V ($Å^3$)
x = 0.00	Rhombohedral (R-3c)	$a = b = c$ = 5.45866 (Å) α = β = γ = 60.4735 (°)	116.243
x = 0.25	Rhombohedral (R-3c)	$a = b = c$ = 5.45903 (Å) α = β = γ = 60.6003 (°)	116.595
x = 0.50	Monoclinic (P 21/n)	a = 5.36332 (Å) b = 5.46978 (Å) c = 7.74353 (Å) β = 88.6507 (°)	227.103
x = 0.75	Rhombohedral (R-3c)	$a = b = c$ = 5.39213 (Å) α = β = γ = 60.7529 (°)	112.741
x = 1.00	Rhombohedral (R-3c)	$a = b = c$ = 5.37493 (Å) α = β = γ = 60.7199 (°)	111.584

Table 2. the values of crystallite size and strain of $LaMn_{1-x}Co_xO_3$ obtained from Scherrer and H-W methods.

Sample	$D_{m\text{-}Sch}$ (nm)	$D_{H\text{-}W}$ (nm)	$\varepsilon_{H\text{-}W}*10^3$ (no unit)
x = 0.00	28.89	32.36	2.42
x = 0.25	28.45	29.58	2.12
x = 0.50	19.5	23.47	5.48
x = 0.75	14.48	27.55	10.56
x = 1.00	40.91	28.73	5.68

Table 3. Magnetic results of $LaMn_{1-x}Co_xO_3$.

Sample	M_S(10 K) (emu/g)	H_C (10 K) (Oe)	M_r (10 K) (emu/g)	T_C (K)
x = 0.00	8.96	90	1.50	130
x = 0.25	7.34	2730	3.48	184
x = 0.50	4.21	4310	2.32	230
x = 0.75	1.29	5040	0.30	179
x = 1.00	0.54	4310	0.23	169

Table 4. Catalytic performance (%),the C_2H_6 combustion and CO oxidation temperatures (°C) for $LaMn_{1-x}Co_xO_3$.

Sample	Temperature of CO conversion (˚ C)			Temperature of C_2H_6 conversion (˚ C)		
	10%	50%	90%	10%	50%	90%
x = 0.00	255	295	350	260	358	483
x = 0.25	175	195	298	237	376	404
x = 0.50	127	160	190	177	283	393
x = 0.75	160	179	213	180	374	430
x = 1.00	220	330	380	178	576	702

Several considerations can be forwarded, however, at this stage: first of all, it can be expected that for x ≤ 0.50, when substituting Mn^{3+} by cobalt ions, this ion enters as Co^{2+}, leading to the formation of an equivalent amount of Mn^{4+} to preserve the electro-neutrality of the lattice. In such a case, the mean ionic radius of the B cation must show an increase, with an accompanying increase of the lattice volume (Table 1). It is known that the mean ionic radius of Mn^{4+}-Co^{2+} is larger than that of Mn^{3+}-Co^{3+} [14]. Therefore, the increase in lattice volume has been attributed to the assumption of substituting Co^{2+} by Mn^{3+} due to the larger mean ionic radius of Mn^{4+}-Co^{2+} compared to Mn^{3+}-Co^{3+}. For x > 0.50, a large reduction of the lattice volume (Table 1) correlates well with the presence of Co ions as Co^{3+} in a low spin (LS) state, for which the ionic radius is lower than the corresponding high spin (HS) state (Co^{3+}: HS, 0.61 and LS, 0.545Å). In such a case, the mean ionic radius of the B-site decreases, with an accompanying decrease of the lattice volume (Table 1). Again, this hypothesis is confirmed by the magnetic and catalytic data presented further in this work. For this, a correlation with the magnetic data is necessary, as will be discussed later in this work.

The influence of substitution on the crystal structure can be described by a tolerance factor ($t = r_{A-O}/(\sqrt{2}\ r_{B-O})$) introduced by Goldschmidt to estimate the deviation from the ideal structure. As a result, for x ≤ 0.50, as $<r_{B-O}>$ increases, *t* decrease, at first the rhombohedral structure for x = 0.0 is further distorted to the rhombohedral structure for x = 0.25 and then for x = 0.50 the structure transforms to monoclinic in which the bending of the B-O-B bond increases and the bond angle deviates from 180°. For x > 0.50 inversely, as $<r_{B-O}>$ decreases, *t* increase, the lattice structure transforms from a monoclinic to a rhombohedral structure.

The results for the crystallite sizes obtained from the mean value of 15 strongest peaks shown in Fig. 1 for both structures by using the Scherrer method are summarized in Table 2.

The Halder-Wagner method was used to study the individual contributions of crystallite size and lattice micro-strain on isotropic line broadening of 15 strongest peaks of the $LaMn_{1-x}Co_xO_3$ compounds.

In this method, the plot of $\left(\frac{\beta^*_{hkl}}{d^*_{hkl}}\right)^2$ (axis y) versus $\left(\frac{\beta^*_{hkl}}{d^*_{hkl}{}^2}\right)$ (axis-x) is a straight line (see Fig. 2).

The crystallite size is determined from the slope inverse of the linearly fitted data and the root of the y-intercept gives the strain, respectively. The results of crystallite size and micro-strain of $LaMn_{1-x}Co_xO_3$ (x = 0.00, 0.25, 0.50, 0.75, 1.00) estimated by the Scherrer and H-W methods are summarized in Table 2. The values for x = 0.50, 0.75 are less than for the other samples.

The H-W method supposes that the ‘‘crystallite size” profile contributes to the line broadening by a Lorentzian function and the ‘‘strain” profile by a Gaussian function. This method shows that line broadening is essentially isotropic. However, the advantage of the H-W method over the Scherrer method is that less weight is given to the data from reflections at high angles where the precision is usually lower [10].

However, the mean crystallite size obtained from the Scherrer formula and the H-W analysis (see Table 2) show a greater variation because of the difference in averaging of the particle size distribution and the results of the H-W method are more accurate, with all the data points touching the fitting line. It is noted that the crystallite size obtained from this method is a minimum at about x = 0.50.

Fig. 3 shows the FTIR spectrum of $LaMn_{1-x}Co_xO_3$ (x = 0.00, 0.25, 0.50, 0.75, 1.00). The presence of metal oxygen bonds i.e. symmetrical lengthening of the *O-B-O* and asymmetrical lengthening of the B-O bond of the octahedron BO_6 structures could be revealed from the peaks at 410 and 600 cm^{-1}, respectively. The widening of the 600 cm^{-1} band and/or the appearance of a shoulder indicates a structure with a lower symmetry [6].

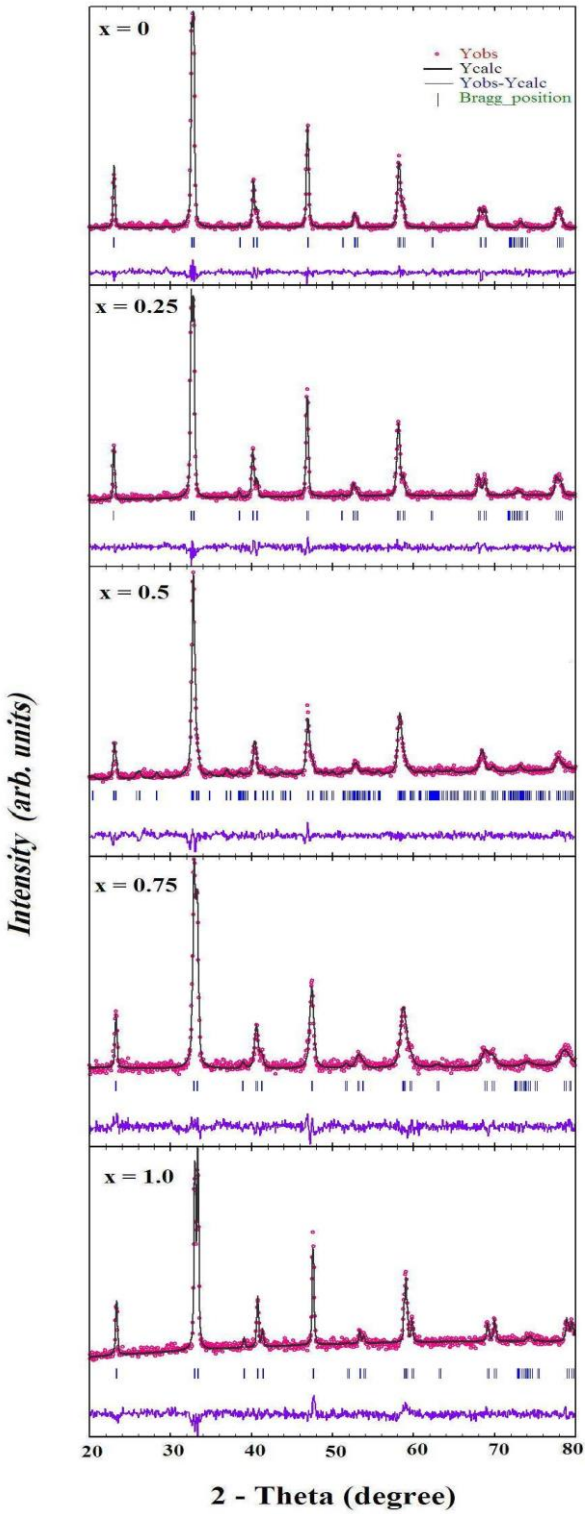

Fig. 1. Rietveld analysis of the X-ray diffraction patterns for $LaMn_{1-x}Co_xO_3$ (x = 0.00, 0.25, 0.50, 0.75, 1.00). The circle signs represent the raw data. The solid line represents the calculated profile. Vertical bars indicate the position of Bragg peaks for samples with the rhombohedral structure (Space Group R -3 c) and for the sample x = 0.5 with the monoclinic structure (Space Group $P2_1/n$). The lowest curve is the difference between the observed and the calculated patterns. The X-ray diffraction patterns for all samples at about 33 ° are shown in the inset of x = 0.75.

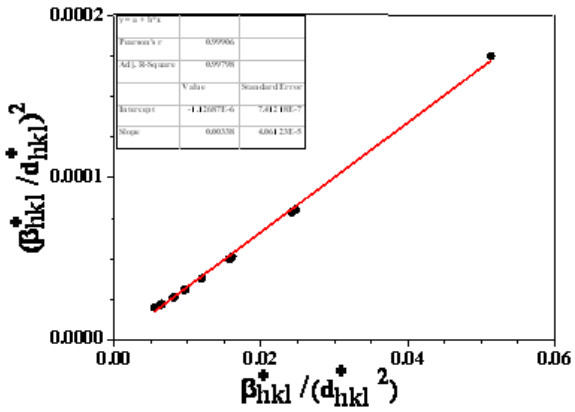

Fig. 2. Fitted curves of the Halder-Wagner analysis for x = 0. The *y*-intercept gives the mean value of the strain and the slope gives the crystallite size.

Therefore, for the perovskites with x < 0.50, the spectra corresponds to a rhombohedral structure with a great symmetry but for x > 0.50, a shoulder appears at 550 cm^{-1} and is characteristic of a rhombohedral structure with a lower symmetry. The peak at 410 cm^{-1} can be attributed to a lower symmetry in three samples x = 0.50, 0.75, 1.00. These results are in accordance with the unit cell parameter α obtained from the XRD analysis so that the larger α, shows a lower symmetry. The narrow band at 1385 cm^{-1} might correspond to the CO_3^{2-} groups.

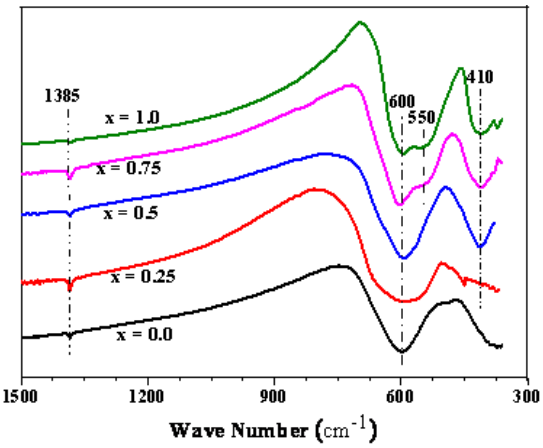

Fig. 3. FT-IR spectra for $LaMn_{1-x}Co_xO_3$.

A similar morphology is observed in SEM micrographs of the samples for $LaMn_{1-x}Co_xO_3$ (x = 0.0, 1.0) as shown in Fig. 4. The TEM micrographs and particle size distribution of samples at x = 0.0 and 1.0 are shown in Fig. 4. Size distribution histograms are fitted by using a log-normal function as follow:

$$P(d) = \frac{1}{d\sigma_d\sqrt{2\pi}}\exp\left\{-\frac{1}{2\sigma_d^2}ln^2\left(\frac{d}{d_{TEM}}\right)\right\}, \quad (6)$$

where σ_d is the standard deviation of the diameter and d_{TEM} is the mean diameter obtained from the

TEM results. The mean diameter was calculated to be 36 nm (x = 0.0) and 50 nm (x = 1.0), respectively. These results are different from the calculated crystallite sizes from the XRD line profile. The differences are related to the irregular shape of the nanoparticles with spherical and polygon morphologies which are observed in the TEM micrographs [8].

Magnetic properties

The hysteresis loops of the $LaMn_{1-x}Co_xO_3$ (x = 0.00, 0.25, 0.50, 0.75, 1.00), shown in Fig. 5, are compared at 10 K, measured in a SQUID magnetometer (Quantum Design, Inc.). The curves of M_H , and S-shaped hysteresis loops show the coercivity field H_C (intersection with the x axis), remanance magnetization M_r (intersection with the x axis) and the saturation magnetization M_S. The values of H_C, M_r and M_S as calculated are summarized in Table 3. The increase of H_C with cobalt content has been attributed to the increase of the magnetic domains. The M_r and M_S values for samples $x \leq 0.50$ are larger than $x > 0.50$.

The temperature dependence of magnetization in the range 5-400 K under the applied magnetic field 0.1T for $LaMn_{1-x}Co_xO_3$ (x = 0.00, 0.25, 0.50, 0.75, 1.00) is shown in Fig. 6. The Curie temperature obtained from the critical point in the derivative of the M-T curves is mentioned in Table 3 that clearly displays a non-monotonic dependence of T_C with the Co doping level. In Co doped samples, the interval of T_C is about 50 K for each addition of 0.25 cobalt concentration. Firstly, the transition temperature, T_C, increases with x and then decreases as x increases. The compound $LaMn_{0.5}Co_{0.5}O_3$ characterized by the presence of two ferromagnetic phases with T_C = 225 and 150K is subject to the synthesis conditions [15]. The former magnetic phase is formed at 700 ˚C, whereas the latter phase can be obtained by quenching from 1300 ˚C. A high-spin order Co^{2+}–Mn^{4+} valence state and low-spin disorder-nonmagnetic Mn^{3+}-Co^{3+} ions were discovered for samples with higher and lower Curie temperatures, respectively. In addition, the Co^{2+} and Mn^{4+} ions are ferromagnetically aligned and the average ionic radii of Mn^{4+}-Co^{2+} are larger than those of Mn^{3+}-Co^{3+} and the high temperature samples $LaMn_{0.5}Co_{0.5}O_3$ are characterized by a smaller volume [14].

The pure manganite $La^{3+}Mn^{3+}O^{2-}{}_3$ (x = 0) is essentially antiferromagnetic [13] with an orthorhombic structure, while in our case, there is a ferromagnetic component with a low coercive field and large magnetization values. A recent study [16] showed that stoichiometric $LaMnO_3$ should be prepared in the absence of oxygen but sintering in ambient air results in nonstoichiometric $LaMnO_{3+\delta}$ with the formation of Mn^{4+} ions larger than 20%.

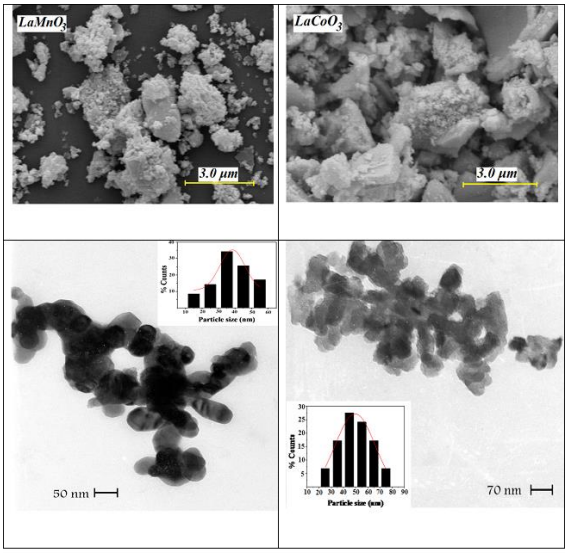

Fig. 4. SEM results, TEM micrographs and size distribution histograms for $LaMn_{1-x}Co_xO_3$.

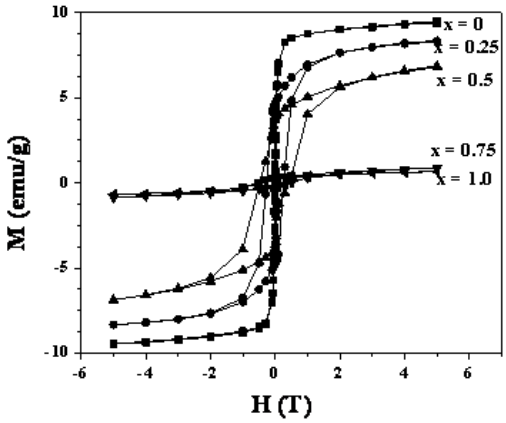

Fig. 5. The hystersis loops (M-H) at 10 K for $LaMn_{1-x}Co_xO_3$.

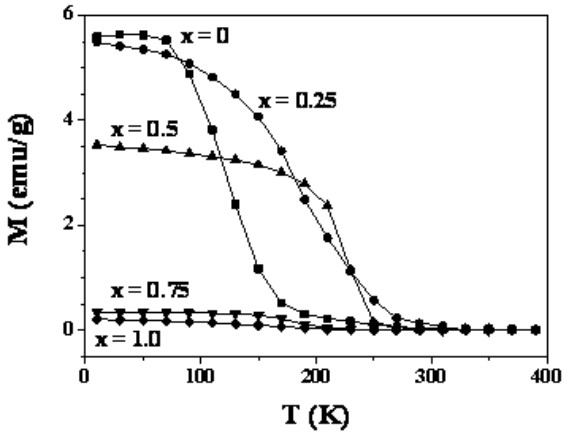

Fig. 6. The magnetization curves versus temperature measured under an applied magnetic field 0.1T for $LaMn_{1-x}Co_xO_3$.

For our sample $LaMnO_3$ annealed in the presence of oxygen, the room temperature structure is rhombohedral and indicates the percentage of Mn^{4+} is larger than 20%. Therefore, the magnetization values observed in the studied $LaMnO_3$ sample can be related to a double exchange of Mn^{4+}- Mn^{3+}. In addition, all the samples are definitely ferromagnetic. The M_S values for $x \leq 0.50$ are larger than $x > 0.50$. It is known that the interactions of Co^{2+}-Co^{3+} and Co^{3+}-Mn^{3+} are of the anti-ferromagnetic type and Co^{2+}-Mn^{3+} and Mn^{4+}-Mn^{3+} are ferromagnetic [6]. In accordance with the structural results, the large magnetization values for $x \leq 0.50$ suggests a substitution of Co^{2+} with Mn^{3+} reaching a maximum at x = 0.50, for which the charge equilibrium equation is $La^{3+}Mn^{4+}{}_{0.5}Co^{2+}{}_{0.5}O^{2-}{}_3$. While for $x > 0.50$, the magnetization decreases by several orders of magnitude, meaning that the ferromagnetic interactions of Co^{2+}–Mn^{4+} are weaker (the quantity of Mn cations decreases), being progressively replaced by the less effective Co^{2+}–Co^{3+} and Mn^{4+}-Co^{3+} interactions. Therefore, again the hypothesis presented from structural calculations is confirmed by the magnetic data. Catalytic performance (%) curves of C_2H_6 combustion and CO oxidation reactions for $LaMn_{1-x}Co_xO_3$ with x = 0.00, 0.25, 0.50, 0.75 and 1.00 are shown in Figs. 7, 8. Also, catalytic performance tests of $LaMn_{1-x}Co_xO_3$ catalysts at 10%, 50% and 90% of C_2H_6 combustion and CO oxidation are summarized in Table 4. The changes in the catalytic properties of A(B, B')O_3 perovskite in substitution of cation B with B' can be classified in two categories: geometric and electronic structure of the cation B'. The effect of Co substitution on the geometric factors is considered in the calculation of factor *t* that should be related to the structural changes summarized in Table 1. It is suggested that

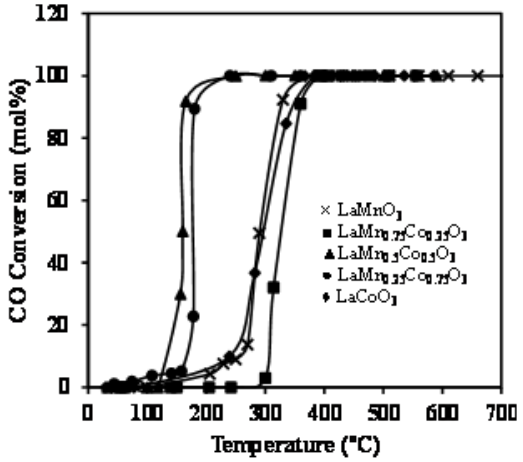

Fig. 7. Catalytic performance curves of $LaMn_{1-x}Co_xO_3$ for CO oxidation.

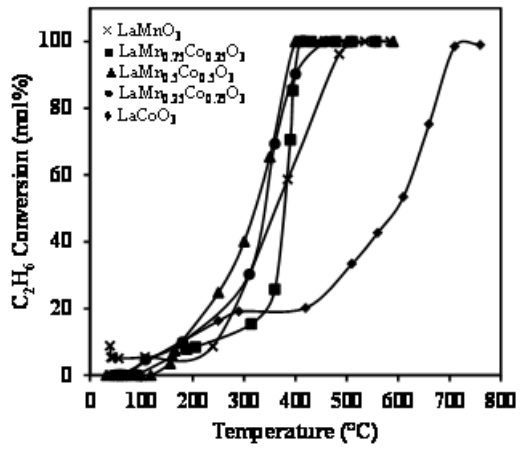

Fig. 8. Catalytic performance curves of $LaMn_{1-x}Co_xO_3$ for the C_2H_6 combustion.

Catalytic Properties

the decrease in the tolerance factor will be lower than the *B*-O-*B* bond strength and promotes the formation of oxygen vacancies at the surface [7]. Therefore, it is expected that the samples x = 0.50, 0.75 show a higher activity for C_2H_6 combustion and CO oxidation reactions.

There is an inverse relationship between the crystallite size and the specific surface area of the samples. In addition, it is known that the higher activity should be related to the higher specific surface and lower crystallite sizes. Consequently, we can conclude that the higher activity of the samples x = 0.50, 0.75 can be attributed to a lower crystallite size.

The band gap energies calculated for $LaMn_{1-x}Co_xO_3$ compounds with x = 0.00, 0.25, 0.50, 0.75, and 1.00 are 1.58, 1.23, 0.98, 1.13, and 0.99, respectively. These values of the band gap energy show a semiconducting behavior of the samples. The low band gap energy of the compounds contributes to their high catalytic activities.

Also, the results of the catalytic characterization should be related to the electronic configuration which intervenes directly in the structural and magnetic changes formed. In ABO_3 perovskites, a simple way of varying the oxidation state of the B^{3+} ion is by substitution of the A^{3+} ion by a different one with an oxidation state other than 3. For example, in (La, M)CoO_3 systems, the appearance of Co^{4+} ions by substitution with M = Sr decreases the rate, whereas the presence of Co^{2+} ions by introduction of M = Ce^{4+} enhances the rate of the oxidation reaction of CO and the hydrocarbons[5]. Therefore, the noticeable higher activity of x = 0.25, 0.50 and 0.75 perovskites is attributed to the presence of Co^{2+}, as pointed out for hole doped (La, M) CoO_3 systems in reducing the atmosphere,

compared to pure cobaltite [5]. The larger Co^{2+} cation than Co^{3+} results in a shorter Co-O bond (see Fig. 3). Thus, lattice oxygens participate more easily in the redox process and therefore reduce the conversion temperature of C_2H_6 combustion and CO oxidation. This behavior is explained considering that at high x values, the amount of unstable Co^{4+} ions and/or of oxygen vacancies increases, which favors the diffusion of lattice oxygen from the bulk to the surface, as charge compensators. As a consequence of the above discussions, C_2H_6 combustion and CO oxidation take place at a lower temperature over the x = 0.50 catalyst compared with the other samples.

Some reports have shown volcano-type dependence between the activity of C_2H_6 combustion and CO oxidation and the electronic configuration of the transition metal ions B [5, 7]. According to crystal field theory, the octahedral environment of the B^{3+} ions splits into two lower and higher energy levels t_{2g} and e_g, respectively. The maximum activity in the volcano curves is attained for an occupation of the e_g levels of less than one electron whereas the t_{2g} levels remain half-filled or completely filled [5]. Also, the Mn^{4+} ion configuration in these manganites with the half filled t_{2g} orbitals and empty d_{z^2} orbitals shift the Fermi level towards the centre of the antibonding e_g orbitals at the surface, which promotes CO and C_2H_6 chemisorptions at the surface leading to C_2H_6 combustion and CO oxidation [7, 8]. Finally, we may conclude from the structural, magnetic, and catalytic variations of the sample at x = 0.50 that the spin states of the Co^{2+} and Mn^{4+} ions may be in low spin $t_{2g}^6 e_g^1$ and t_{2g}^3, respectively.

CONCLUSIONS

The structural characterization of $LaMn_{1-x}Co_xO_3$ (x = 0.00, 0.25, 0.50, 0.75, 1.00) by X-ray powder diffraction and FTIR measurments is evidence for a monoclinic structure (P21/n space group) with x = 0.50 and a rhombohedral structure (R-3c space group) for other samples without the presence of impurity phases. The unit cell volume obtained from the Rietveld method shows increasing and decreasing tendencies for the values $x \leq 0.5$ and $x > 0.5$, respectively. The structural and magnetic results suggest Co^{2+} and Co^{3+} substitution with Mn ions for $x \leq 0.50$ and $x > 0.50$, respectively. The results also show that the sample for x = 0.50 has a lower symmetry, smaller crystallite size (bigger surface area) and a higher content of Co^{2+} than the other samples which make it the best catalyst for C_2H_6 combustion and CO oxidation.

Acknowledgment: *The authors wish to thank Frances Hellman, from the University of California-Berkeley for her help with the magnetic measurements.*

REFERENCES

1. P. Ciambelli, S. Cimino, S. De Rossi, L. Lisi, G. Minelli, P. Porta, G. Russo, *Appl. Catal. B.*, **29**, 239 (2001).
2. H. Tanaka, M. Misono, *Solid. State. Mater. Sci.*, **5**, 381 (2001).
3. C. Zener, *J. Phys. Rev.*, **81**, 440 (1951).
4. J. B. Goodenough, *J. Phys. Rev.*, **100**, 564 (1955).
5. M. A. Peña, J. L. G. Fierro, *Chem. Rev.*, **101**, 1981 (2001),
6. G. Pecchi, C. Campos, O. Peña, L. E. Cadus, J. Mol. *Catal. A: Chem*., **282**, 158 (2008).
7. R.G. Shetkar, A.V. Salker, Electrical, *J. Mater. Sci. Technol.*, **26**, 1098 (2010).
8. E. Frozandeh-Mehr, A. Malekzadeh, M. Ghiasi, A. Gholizadeh, Y. Mortazavi, A. Khodadadi, *Catal. Commun.*, **28**, 32 (2012).
9. M. Khazaei, A. Malekzadeh, F. Amini, Y. Mortazavi, A. Khodadadi, *Cryst. Res. Technol.*, **45**, 1064 (2010).
10. A. Gholizadeh, *J. Adv. Mater. Process.*, **3**, 71 (2015).
11. A. Gholizadeh, N. Tajabor , *Mater. Sci. Semicond. Process.*, **13**, 162 (2010).
12. R. Groessinger, *Phys. Stat. Sol. (a)*, **66**, 665 (1981).
13. G. Pecchi, C. Campos, O. Peña, *Mater. Res. Bull.*, **44**, 846 (2009).
14. G.V. Bazuev, A.V.Korolyov , M.A.Melkozyorova, T.I. Chupakhina, *J. Magn. Magn. Mater.*, **322**, 494 (2010).
15. P. A. Joy, Y. B. Khollam, S. K. Date, *Phys. Rev. B*, **62**, 8608 (2000).
16. Y.D. Zhao, J. Park, R. J. Jung, H. J. Noh, S. J. Oh, *J. Magn. Magn. Mater.*, **280**, 404 (2004).

СТРУКТУРНИ, МАГНИТНИ И КАТАЛИТИЧНИ СВОЙСТВА НА КОБАЛТ-ЗАМЕСТЕНИ МАНГАНТИНИ ПЕРОВСКИТИ

А. Голизаде[1], А. Малекзаде[2], М. Гиаси[2]

[1]*Училище по физика, Университет Дамган, Дамган, И.Р. Иран*
[2] *Училище по химия, Университет Дамган, Дамган, И.Р. Иран*

Постъпила на 4 август, 2015 г.; коригирана на 22 октомври, 2015 г.

(Резюме)

В тази работа са изследвани структурните, магнитните и каталитичните свойства на $LaMn_{1-x}Co_xO_3$ (x = 0.00, 0.25, 0.50, 0.75, 1.00). Структурното охарактеризиране на образците чрез прахова рентгено-структурна дифракция и с помощта на пакет от програми X'Pert и Fullprof доказва моноклинна структура (P21/n пространствена група) с x = 0.5 и ромбоедрична структура (R-3c пространствена група) за други проби. Тези резултати се потвърждават с FTIR-измервания. Магнитните характеристики на пробите са определени с измервания при различни температури и полета. Структурните и магнитните резултати показват, че феромагнитните взаимодействия Co^{2+}–Mn^{4+} при $x \leq 0.5$ прогресивно се заменят с по-малко ефективните взаимодействия Co^{2+}–Co^{3+} и Mn^{4+}-Co^{3+} за $x > 0.5$. Каталитичната активност на $LaMn_{1-x}Co_xO_3$ са оценени за реакциите на изгаряне на C_2H_6 и окислението на CO. При сходни условия резултатите от катализата показват, че нано-перовскитът $LaMn_{0.5}Co_{0.5}O_3$ е най-добрия катализатор за тези две реакции.